JBC COMMUNICATION

NMR characterization of an assembling RHIM (RIP homotypic interaction motif) amyloid reveals a cryptic region for self-recognition

Received for publication, January 31, 2023, and in revised form, February 25, 2023 Published, Papers in Press, March 2, 2023,
https://doi.org/10.1016/j.jbc.2023.104568

Chi L. L. Pham[1,‡], **Gustavo A. Titaux-Delgado**[2,‡], **Nikhil R. Varghese**[1,‡], **Paula Polonio**[2], **Karyn L. Wilde**[3], **Margaret Sunde**[1], **and Miguel Mompeán**[2,*]

From the [1]School of Medical Sciences, Sydney Nano and Sydney Infectious Diseases, University of Sydney, Sydney, New South Wales, Australia; [2]"Rocasolano" Institute of Physical Chemistry, Spanish National Research Council, Madrid, Spain; [3]National Deuteration Facility Australian Nuclear Science and Technology Organization (ANSTO), Sydney, New South Wales, Australia

Reviewed by members of the JBC Editorial Board. Edited by Wolfgang Peti

The RIP homotypic interaction motif (RHIM) is an essential protein motif in inflammatory signaling and certain cell death pathways. RHIM signaling occurs following the assembly of functional amyloids, and while the structural biology of such higher-order RHIM complexes has started to emerge, the conformations and dynamics of nonassembled RHIMs remain unknown. Here, using solution NMR spectroscopy, we report the characterization of the monomeric form of the RHIM in receptor-interacting protein kinase 3 (RIPK3), a fundamental protein in human immunity. Our results establish that the RHIM of RIPK3 is an intrinsically disordered protein motif, contrary to prediction, and that exchange dynamics between free monomers and amyloid-bound RIPK3 monomers involve a 20-residue stretch outside the RHIM that is not incorporated within the structured cores of the RIPK3 assemblies determined by cryo-EM or solid-state NMR. Thus, our findings expand on the structural characterization of RHIM-containing proteins, specifically highlighting conformational dynamics involved in assembly processes.

Polymerization into higher-order supramolecular complexes is essential to mammalian innate immunity pathways (1). Upon recognition of pathogen- or danger-associated molecular patterns, death domains (DDs), Toll/IL-1 receptor (TIR) domains, and RIP homotypic interaction motifs (RHIMs) assemble homotypically (*i.e.*, DD with DD, or RHIMs with RHIMs) to signal for distinct immune responses, from proinflammatory cytokine production to activation of transcription factors and to cell death. Mechanistic insights can now be inferred by contrasting the structures of these proteins in their monomeric and in their complexed, active states (2). This has established that while DDs do not undergo structural changes upon assembly (2), TIR domains exhibit rearrangements at the TIR:TIR contact surfaces while the native flavodoxin-like fold is maintained (3, 4). Unlike DD- and TIR-mediated assembly, which consists of well-folded domains arranged into ring-shaped or filamentous higher-order assemblies, RHIM-mediated polymerization occurs through a dramatically different mechanism, namely amyloid signaling (5), with the formation of β-structure concomitantly with recruitment of monomers into the fibrillar form. This assembly concentrates other functional, folded domains within the signaling complex. The amyloid-forming domains of two RHIM-containing proteins, RIPK1 and RIPK3, have been structurally studied in the complexed, fibril state (6, 7), whereas the monomeric state of these proteins remains structurally elusive.

The RIPK3 RHIM was reported in 2002 as a hydrophobic stretch comprising 16 residues (448–464), and key to the interaction with RIPK1, although residues outside this RHIM core region were also shown to be required for the mutual interaction of the RIPK1 and RIPK3 RHIMs (8). The RIPK3 RHIM was predicted then to adopt a β-hairpin with a turn composed of residues 454 to 457 (8). Solid-state NMR (SSNMR) and cryo-electron microscopy (cryo-EM) data collected on RIPK3 amyloids formed by a longer C-terminal construct (residues 387–518) consistently detect only residues within the core of the RHIM, supporting the prediction that the remaining parts of the protein C-terminal region are unstructured (6, 7). The lack of structural information on RHIM monomers and the mechanism of RIPK3 incorporation into the amyloid form poses a major limitation to understanding initiation of RHIM-mediated innate immunity pathways and programmed cell death.

Both SSNMR and cryo-EM structural models of RIPK3 homo-amyloids established that the RIPK3 RHIM adopts essentially identical conformations in fibrils assembled in acetate buffer (at pH 4–5) or under quasi-physiological conditions (in phosphate buffer at pH 7) (7). In this Communication, we report successful reconstitution and characterization of tag-free, soluble RIPK3 (387–518) under both amyloid-forming and nonamyloid-forming conditions, identifying the RHIM-encompassing region of RIPK3 C-terminal to the kinase domain as intrinsically disordered in the

‡ Co-first authors.
* For correspondence: Miguel Mompeán, mmompean@iqfr.csic.es.
Present address for Chi L.L. Pham: School of Natural Sciences, Macquarie University, Sydney, NSW 2109, Australia.

monomeric soluble form, contrary to predictions, and affording identification of the set of residues involved in the assembly of RIPK3 into the amyloid form associated with necroptosis signaling.

Results

Building on prior studies that reported essentially identical RIPK3 fibril structures in acetate buffer (at acidic pH) and in phosphate buffer (at quasi-physiological pH) (7), we sought to characterize the monomeric form of RIPK3 (387–518) over this pH range in solution. To this end, lyophilized, isotopically ^{13}C, ^{15}N-labeled RIPK3 (387–518) monomer was dissolved in 8 M urea (pH adjusted to 6.5 or to 4.0) to ensure full solubilization, and then buffer exchanged using gel filtration to remove the denaturant, into 90:10 H_2O/D_2O solutions containing 20 mM 2-(N-morpholino)ethanesulfonic acid (MES) (final pH adjusted to 6.5) or 1 mM acetic acid (final pH adjusted to 4.0). The ^1H-^{15}N heteronuclear single quantum coherence (HSQC) spectra recorded on these protein samples, whose final concentrations are in the range 18 to 20 μM, revealed the typical pattern of disordered proteins. The peaks map to a narrow region spanning ca. 1 ppm in the ^1H dimension, suggesting that the entire C-terminal domain of RIPK3, including hydrophobic residues within the RHIM, is chiefly disordered (Figs. 1 and S1).

The spectra for the RIPK3 (387–518) sample in 20 mM MES at pH 6.5 (Fig. S2) showed remarkably broader peaks than those corresponding to the sample at pH 4.0 (Fig. 1). In fact, when the pH of this latter sample was smoothly raised from 4.0 to 5.0, 5.5, and finally to 6.5 by small aliquots (0.5 μl each) of 100 mM Na_2CO_3, the corresponding ^1H-^{15}N HSQC spectra revealed no significant peak shift in the RHIM region but instead exhibited a marked decrease in signal intensities (Fig. 2*A*).

These signal losses were quite inhomogeneous throughout the RIPK3 (387–518) sequence, as gauged from the first increment of the corresponding ^1H-^{15}N HSQC spectra (Figs. 2*A* and S1). According to thioflavin T (ThT) assays, the broadening and loss of intensity observed upon raising the pH is consistent with the assembly of amyloid fibrils when the pH is raised to 6.5 from pH 4.0 (Fig. 2*B*).

The RHIM is a hydrophobic stretch within a predicted disordered domain (8), reminiscent of the hydrophobic α-helix within the disordered domain of TAR DNA-binding protein 43 in which electrostatic repulsion at low pH opposes hydrophobic-driven assembly (9). Indeed, the net charge of RIPK3 (387–518) would increase from +3 to +9.8 upon lowering the pH from 6.5 to 4.0, according to computational predictions (https://protcalc.sourceforge.net). Within the framework of such a charge model in which high electrostatic protein–protein repulsion at low pH would prevent assembly, screening of charges by, *e.g.*, NaCl should provoke assembly

G$_{387}$SSSDSMAQPPQTPETSTFRNQMPSPTSTGTPSPGPRGNQGAERQGMNWSCRTPEPNPVTGRP$_{448}$**LVNI YNCSGVQVGDNNYLTM**$_{468}$QQTTALPTWGLAPSGKGRGLQHPPPVGSQEGPKDPEAWSRPQGWYNHSGK$_{518}$

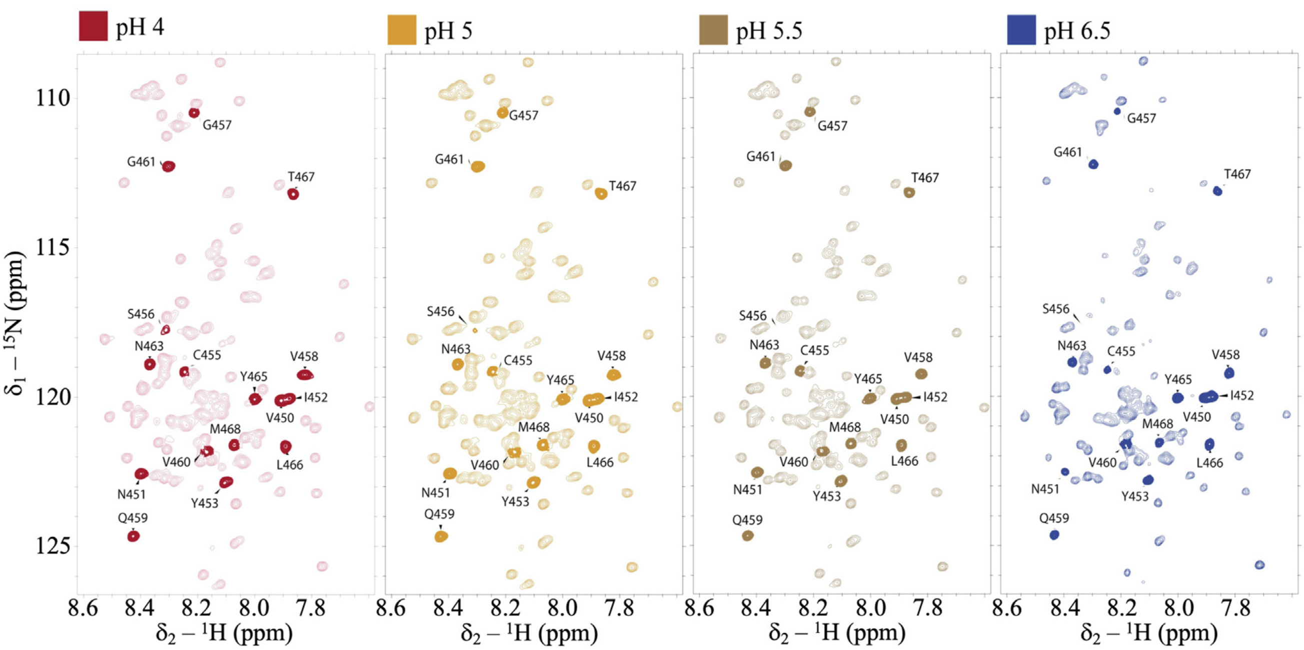

Figure 1. ^1H-^{15}N HSQC spectra of 18 μM RIPK3 (387–518) at 25 °C and different pH values. The protein sequence is displayed on *top* of the spectra, with RHIM residues highlighted in *bold*, acidic residues in *red*, and basic residues in *blue*. Sample was initially prepared at pH 4.0 using 1 mM DAc, and then the pH was raised to 5.0, 5.5, and 6.5 through the addition of 100 mM sodium carbonate, with ^1H-^{15}N HSQC spectra recorded at the various pH values. Note that RHIM residues, which are labeled in every spectrum and depicted with increased saturation for clarity, do not shift upon raising the pH. Fig. S1 shows an overlay of the ^1H-^{15}N HSQC spectra recorded at the four pH values. HSQC, heteronuclear single quantum coherence; RHIM, RIP homotypic interaction motif; RIPK3, receptor-interacting protein kinase 3.

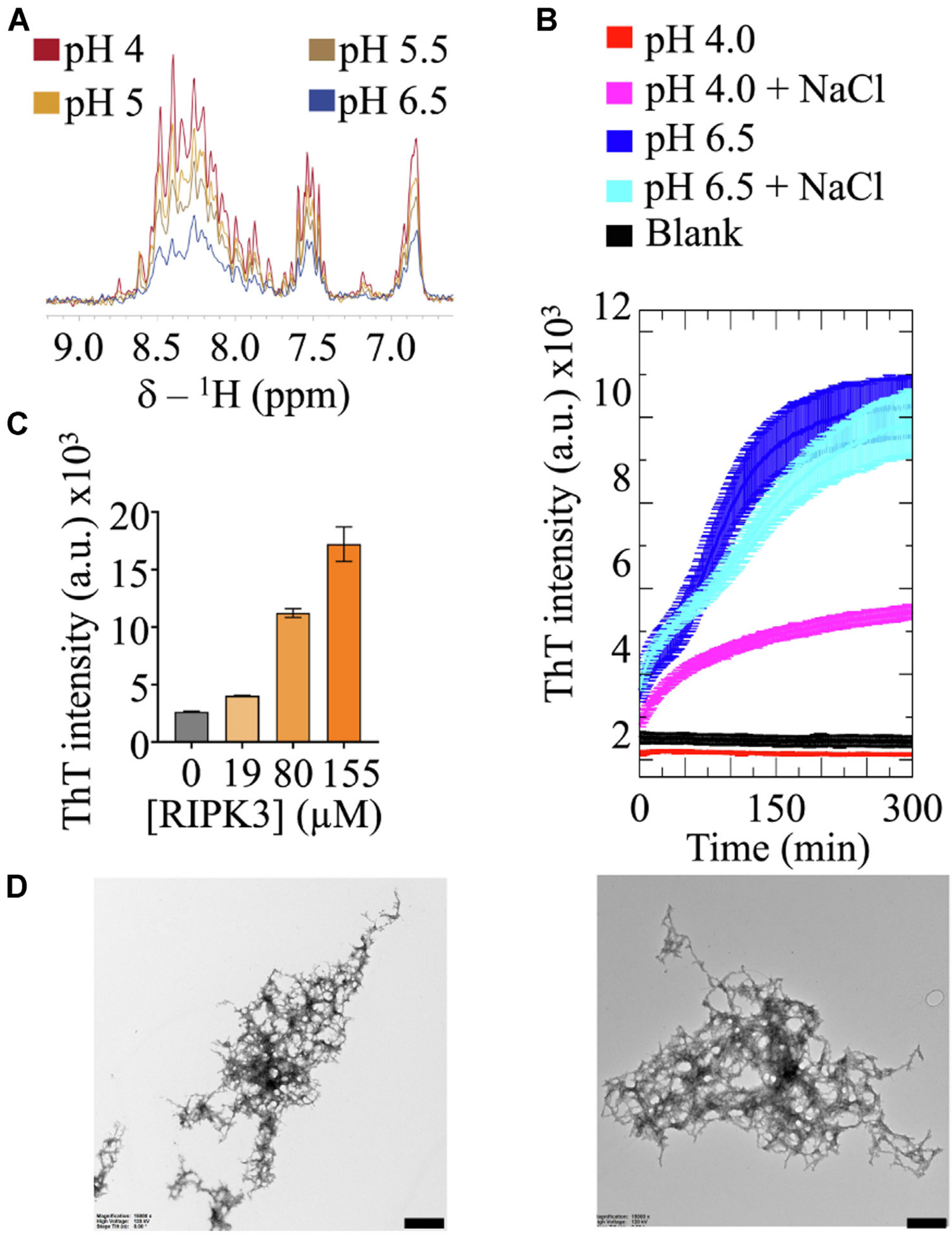

Figure 2. Effect of pH, salt and concentration on RIPK3 amyloid assembly. *A*, first increments of the distinct ^{1}H-^{15}N HSQC NMR spectra of RIPK3 (387–518) at different pH values shown in Figs. 1 and S1. *B*, ThT fluorescence emission over time of 5 μM RIPK3 (387–518) in the absence and presence of 150 mM NaCl, at pH 4.0 and 6.5. *C*, ThT fluorescence emission spectra of RIPK3 (387–518) at different concentrations (pH 4, no NaCl). *D*, electron micrograph of fibrils from (*left*) 100 μM RIPK3 (387–518) at pH 4.0 (0 mM NaCl, in the presence of preformed seeds)) and (*right*) 5 μM RIPK3 (387–518) at pH 6.5 (150 mM NaCl, in the absence of preformed seeds). Scale bar 100 nm. HSQC, heteronuclear single quantum coherence; RIPK3, receptor-interacting protein kinase 3; ThT, thioflavin T.

just as in the pH 6.5 condition. Figure 2*B* shows that, indeed, the addition of 150 mM NaCl promotes RIPK3 (387–518) assembly into amyloid fibrils at pH 4.0 as indicated by the rapid increase in ThT fluorescence intensity. Moreover, at pH 6.5, the addition of NaCl did not have such a marked effect on the extent or rate of assembly (Fig. 2*B*).

Previous cryo-EM and SSNMR studies have shown that at a high protein concentration (>300 μM), RIPK3 formed homo-amyloid fibrils at low and higher pH values (7). By contrast, our present work here shows that at a low protein concentration, RIPK3 did not form fibrils at pH 4.0 in the absence of NaCl (Figs. 2, *B* and *C* and S3). We reasoned that at high protein concentrations, hydrophobic-driven protein assembly would balance the electrostatic repulsion present at low pH. Using ThT assays and transmission electron microscopy, we confirmed that even at low pH and in the absence of NaCl, RIPK3 readily assembles into fibrils as soon as the concentration is raised (Fig. 2, *C* and *D*), thus reconciling with the cited prior literature (7). Additionally, we observed that RIPK3 fibril assembly is possible at pH 4.0 in the absence of NaCl and at low protein concentration if fibril seeds are present (Figs. 2*D* and S4). The fibrils display an increased tendency to associate into thicker bundles with increasing pH and the presence of NaCl, likely due to reduced electrostatic repulsion (Figs. 2*D* and S4). These results suggest that nucleation of fibril assembly is hindered at pH 4.0, where electrostatic repulsion is strong, but elongation and growth of fibrils is possible if the nucleation barrier is overcome, whereas nucleation and elongation both occur more readily when NaCl is present or at high protein concentration.

The results from Figures 1 and 2 present a way to contrast RIPK3 under amyloid-assembling and under nonamyloid-assembling conditions. In other words, RIPK3 at low pH and at low concentrations (18 μM) represents a nonassembling state, whose assembly into amyloids can be triggered by either addition of NaCl or by raising the pH. Alternatively, assembling conditions are also achievable when the protein concentration is raised. Building on this screening of experimental conditions, we sought to accomplish the NMR characterization of RIPK3 (387–518) using concentrated (180–200 μM) samples. All (100%) ^{13}CA, ^{13}CO, and ^{13}CB nuclei, and 98.5% of ^{1}HA were successfully assigned (Fig. 3*A*). Residues P395, P491, and P492 are excluded from the statistics as they are embedded in PP and PPP repeats, respectively.

No signs of secondary structure are detected in the monomeric form of RIPK3 in solution, according to the calculated neighbor-corrected secondary structure propensities (Fig. 3*B*) (10). The lack of structure in this population-weighted ensemble was further established through $^{3}J_{HNHA}$ coupling constants, whose values throughout the sequence matched those typically observed in statistical coils (Fig. 3*C*). This result contrasts with the β-hairpin originally predicted by Sun *et al.* (8), the propensity for secondary structure within the core RHIM region identified by nine different predictors (Fig. 3*D*), and the β-structure seen in the amyloid RIPK1:RIPK3 complex and RIPK3 homo-amyloid fibrils (6, 7). Now, in the era of AlphaFold2 (11), we have revisited the structural predictions for RIPK3 (entry Q9Y572). In particular, for the RHIM-harboring C-terminal domain spanning residues 387 to 518, AlphaFold2 gives very-low per-residue confidence score (below 50), with a slight increase (from 50 to 70, with 70 the confidence threshold of the method) for the RHIM region (residues *ca.* 450–465). This appears to reflect the unstructured nature of the monomeric form of the RHIM and the propensity of the core region to adopt β-structure upon assembly into the amyloid form.

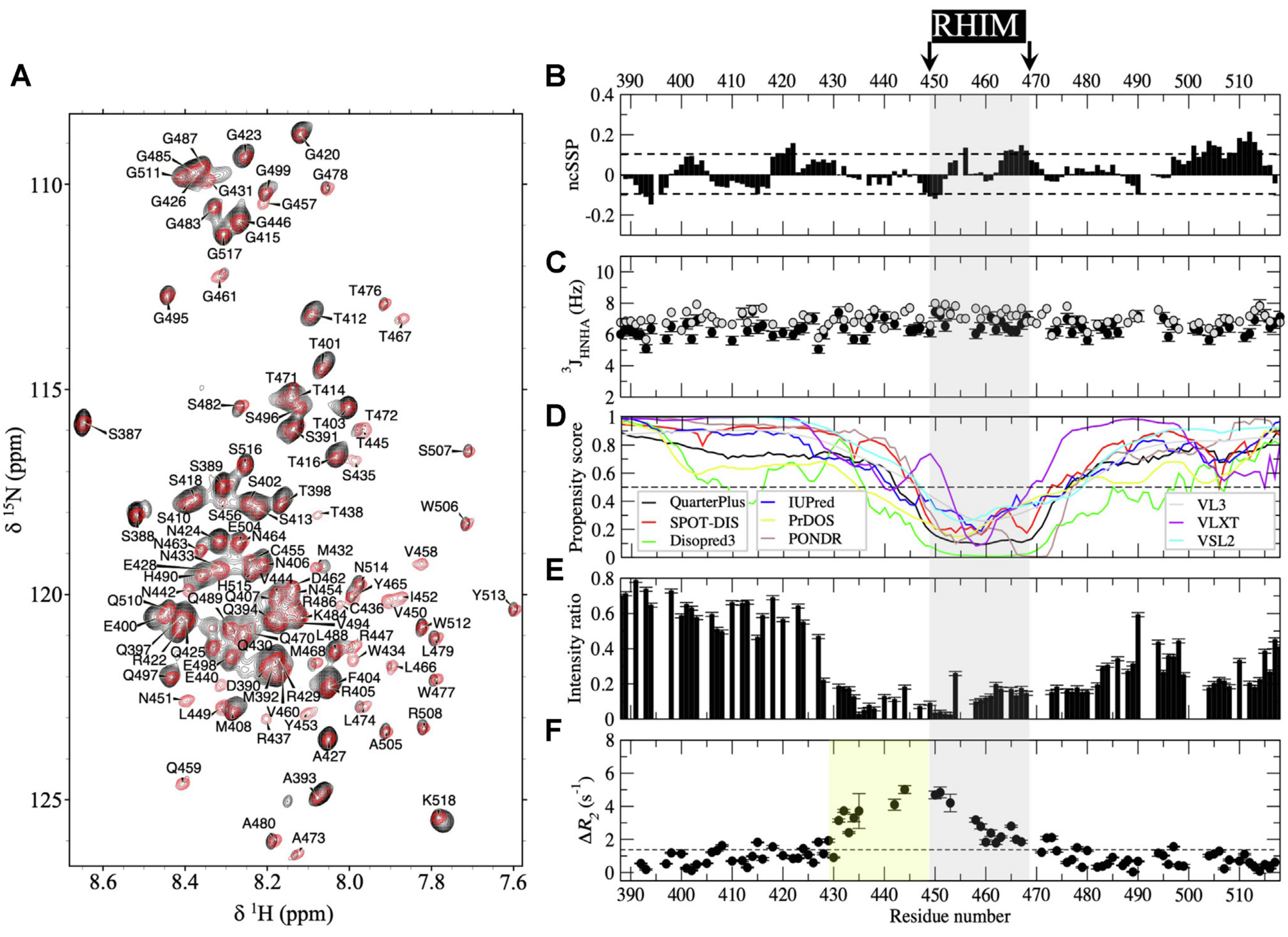

Figure 3. NMR characterization of RIPK3 (387–518). *A*, ^{1}H-^{15}N HSQC spectra of RIPK3 (387–518) at 18 μM (*red*, nonassembling conditions) and 180 μM (*black*, assembling-conditions) recorded on a 800 MHz spectrometer at pH 4.0 and 25 °C. *B*, neighbor-corrected secondary structure propensities. *C*, experimental (*black circles*) and predicted (*gray circles*) statistical coil $^{3}J_{HNHA}$ values. *D*, disorder predictions. *E*, intensity ratio between a concentrated (180 μM, assembling conditions) and a diluted (18 μM, assembling conditions) sample. *F*, ΔR_2 measurements as the difference in R_2 rates obtained under assembling and nonassembling conditions from $R_1\rho$ experiments. HSQC, heteronuclear single quantum coherence; RHIM, RIP homotypic interaction motif; RIPK3, receptor-interacting protein kinase 3.

ASBMB

Despite the lack of a clear propensity toward adopting well-defined structural elements in the monomeric form in solution, the ^{1}H-^{15}N HSQC of aged samples showed peak broadening for residues within the RHIM region (Fig. 3*A*), in agreement with the presence of this motif in the fibril core of RIPK3 amyloids (6, 7). The intensity ratio between these two samples under assembling and nonassembling conditions not only confirmed the site of interaction at the RHIM but also mapped a 20-residue stretch preceding the RHIM (Fig. 3*E*). This result was intriguing, as it suggests that this flanking segment N-terminal to the RHIM may establish protein–protein intermolecular interactions during assembly (Fig. 3*E*), although it remained invisible in cryo-EM or in SSNMR studies of RIPK3-containing fibrils (7).

In order to establish whether monomers use this region preceding the RHIM to directly interact with the fibril surface in the amyloid-bound state, we prepared a ^{15}N-labeled RIPK3 (387–518) sample to obtain the difference in transverse relaxation rates, ΔR_2, under assembling (at 180 μM) and nonassembling (at 18 μM) conditions (Figs. 3*F* and S5). The individual R_2 rates on each sample were derived from $R_{1\rho}$ measurements collected with a 2 kHz spin lock. Under these conditions, the resulting ΔR_2 (*i.e.*, R_2 at 180 μM minus R_2 at 18 μM) identifies which residues in the monomer establish specific contacts with the fibril during the dynamic equilibrium between unbound and amyloid-bound monomers (Fig. 3*F*).

Discussion

The DD-, TIR- and RHIM-mediated assembly of higher-order complexes signals initiation of immunity responses. Unlike DD-mediated and TIR-mediated signaling, RHIM-mediated signaling relies on functional homo-amyloid and hetero-amyloid formation (5, 6, 12). Among RHIM-containing proteins, RIPK3 is particularly important since it is central to the assembly of both canonical and noncanonical amyloid necrosomes to execute necroptosis (13). RHIMs are also involved in apoptosis (14), and an increasing number of viral proteins harboring RHIMs interfere with RHIM-mediated human immunity through the assembly of human:viral hetero-amyloids (12, 15, 16). Our manuscript presents the first NMR assignments of a RHIM in its noncomplexed, monomeric form, and a first map of the conformational changes associated with the conversion of this key protein into a functional amyloid that signals for programmed cell death. Since RIPK3 is the central protein player that transduces input from all three necroptosis pathways into a signal for cell death, such residue-level understanding of its monomer-to-amyloid conversion will contribute to uncover which mechanism operate in inflammation, fungal, bacterial, and viral infections. Our results also provide robust evidence that the paradigmatic RHIM of RIPK3 that is well-structured in assembled, signaling complexes (6, 7) is chiefly disordered in the noncomplexed state. More intriguing, our data reveal that in addition to the RHIM, its preceding ca. 20-residue stretch readily established contacts with the fibril surface in the assembled state. While ongoing efforts will survey the impact of this "pre-RHIM" region in modulating the assembly of both RIPK3 homo-amyloids and hetero-amyloids, it should be stressed that this region has not been detected in any of the previous cryo-EM or SSNMR studies of RIPK3 fibrils, and neither has it been previously investigated in functional necroptosis assays.

Experimental procedures

Protein production and purification

The RIPK3 (387–518) construct was expressed as a $(His)_6$-ubiquitin-RIPK3 fusion protein, with a tobacco etch virus cleavage site between ubiquitin and RIPK3 (387–518). The uniformly ^{13}C and/or ^{15}N-labeled protein was expressed in a 1 l batch culture using a high cell density protocol as described in the Supplementary Information section. For protein purification, cell pellets were resuspended in lysis buffer (20 mM Tris, 150 mM NaCl, 1 mM EDTA, pH 8.0) and sonicated on ice in 45 s bursts 3 to 5 times, followed by centrifugation at 16,000 rpm to obtain insoluble protein pellet. The insoluble protein pellet was solubilized with 6 M GuHCl, 20 mM Tris-HCl pH 8.0, and 5 mM β-mercaptoethanol, and $(His)_6$-ubiquitin-RIPK3 was purified using Ni-NTA agarose (Life Technologies) under denaturing conditions using 8 M urea, 100 mM NaH_2PO_4, 20 mM Tris, 5 mM β-mercaptoethanol at pH 6.5 for washing and at pH 4.0 for elution. $(His)_6$-ubiquitin-RIPK3 (50 μM) was dialyzed out of urea-containing buffer, into 25 mM NaH_2PO_4, 150 mM NaCl, pH 7.4, 0.5 mM DTT, to allow fibril assembly. After dialyzing for 1 h, tobacco etch virus enzyme was added to the sample and dialysis continued for a further 18 to 24 h. This resulted in cleavage of the $(His)_6$-ubiquitin tag from the fusion protein, leaving RIPK3 fibrils. The $(His)_6$-ubiquitin tag was soluble, and the fibrils are insoluble; thus, the two components were separated by centrifugation. RIPK3 insoluble fibrils were then washed three times with water to remove traces of $(His)_6$-ubiquitin. Fibril samples were then incubated in formic acid for 1 h to induce depolymerization and to generate monomeric isotopically ^{13}C, ^{15}N-labeled RIPK3(387–518) RIPK3. This material was lyophilized and stored at −20 °C. NMR samples were subsequently prepared, as indicated in the main text, by direct dissolution in the corresponding buffers either with or without a desalting step.

Thioflavin T fluorescence

All ThT experiments were either performed in a POLARstar Omega microplate reader (BMG Labtech) or using a Jobin-Yvon Fluoromax-4 instrument. In the former case, fluorescence intensity was recorded using a 440 nm (±10 nm) excitation filter and a 480 nm (±10 nm) emission filter. In the latter, 2 nm excitation and emission slit widths were used along with an excitation wavelength of 440 nm and fluorescence emission recorded over the range 450 to 550 nm at a scan speed of 2 nm s^{-1}. Data analysis was performed in Microsoft Excel and GraphPad Prism. Samples were prepared as detailed in the Supporting Information file.

Transmission electron microscopy

Samples for electron microscopy were prepared on formvar–carbon–coated copper grids (200 mesh) (ProSciTech

Pty Ltd) by floating grids on protein-containing droplets for 1 min, then removing excess liquid and subjecting grids to three water washes, before staining by floating on a droplet of 2% uranyl acetate solution, removing excess stain solution, and air-drying overnight. Samples were examined with a FEI Tecnai T12 electron microscope operating at 120 kV. Images captured with a Veleta CCD camera and RADIUS 2.0 imaging software (EMSIS GmbH).

NMR experiments

All NMR experiments were collected at 298 K on a Bruker Avance Neo 800 MHz (^{1}H frequency) spectrometer equipped with a TCI cryoprobe and Z-gradients, on ^{13}C,^{15}N-RIPK3 samples. Samples were prepared by solubilization of the lyophilized material into 8 M urea with 1 mM TCEP, at either pH 4 or pH 6.5 depending on whether they were subsequently desalted into 90/10 H_2O/D_2O containing 1 mM acetic acid (final pH set to 4) or 20 mM MES (final pH set to 6.5), also with 1 mM TCEP in all cases. In the case of the sample at pH 4, the pH was raised to 5.0, 5.5, and 6.5 using small amounts (0.5 μl aliquots) of Na_2CO_3. The concentration of all the samples was estimated to be 18 to 20 μM by UV absorbance. Concentrated samples were prepared by directly dissolving the lyophilized material into 90/10 H_2O/D_2O containing 1 mM acetic acid (final pH set to 4) and 1 mM TCEP (final concentration of samples 180–200 μM). All information regarding pulse sequences employed for backbone and side chain assignments as well as for 15 N relaxation studies are detailed in the Supporting Information file.

Data availability

The dataset generated for this study have been deposited in the Biological Magnetic Resonance Databank (BMRB) and are accessible through accession number 51175 (https://bmrb.io/data_library/summary/index.php?bmrbId=51175).

Supporting information—This article contains supporting information (17–33).

Acknowledgments—We thank Anthony Duff for useful discussions on project design and isotopic labeling.

Author contributions—M. M. conceptualization; C. L. L. P., G. A. T.-D., N. R. V., and P. P. formal analysis; C. L. L. P., G. A. T.-D., N. R. V., P. P., M. S., and M. M. investigation; M. S. and M. M. writing–original draft; M. S. and M. M. supervision; M. M. funding acquisition.

Funding and additional information—This work was supported by Grants PID2020-113907RA-I00 and RYC2019-026574-I from MCIN/AEI/10.13039/501100011033 and "ESF Investing in your future" (M. M.), Grant FJC2021-047976-I funded by MCIN/AEI/10.13039/501100011033 and by European Union Next GenerationEU/PRTR (G. A. T.-D.), and Australian Research Council Discovery Project (DP180101275) and National Deuteration Facility Funding NDF7209 and NDF8102 (M. S.) Research Training Program support to N. R. V. from Australian Government. Cofunded by the European Union (ERC, 101042403 – BiFOLDOME). Views and opinions expressed are however those of the authors only and do not necessarily reflect those of the European Union or the European Research Council. Neither the European Union nor the granting authority can be held responsible for them. NMR experiments were performed in the "Manuel Rico" NMR Laboratory (LMR) of the Spanish National Research Council (CSIC), a node of the Spanish Large-Scale National Facility (ICTS R-LRB). The National Deuteration Facility is partly supported by the National Collaborative Research Infrastructure Strategy – an initiative of the Australian Government.

Conflict of interest—The authors declare that they have no conflicts of interest with the contents of this article.

Abbreviations—The abbreviations used are: cryo-EM, cryoelectron microscopy; DD, death domains; HSQC, heteronuclear single quantum coherence; MES, 2-(*N*-morpholino)ethanesulfonic acid; RHIM, RIP homotypic interaction motif; RIPK3, receptor-interacting protein kinase 3; SSNMR, solid-state NMR; ThT, thioflavin T; TIR, Toll/IL-1 receptor.

References

1. Shi, M., Zhang, P., Vora, S. M., and Wu, H. (2020) Higher-order assemblies in innate immune and inflammatory signaling: a general principle in cell biology? *Curr. Opin. Cell Biol.* **64**, 194–203
2. Nanson, J. D., Kobe, B., and Ve, T. (2019) Death, TIR, and RHIM: self-assembling domains involved in innate immunity and cell-death signaling. *J. Leukoc. Biol.* **105**, 363–375
3. Ve, T., Vajjhala, P. R., Hedger, A., Croll, T., DiMaio, F., Horsefield, S., *et al.* (2017) Structural basis of TIR-domain-assembly formation in MAL- and MyD88-dependent TLR4 signaling. *Nat. Struct. Mol. Biol.* **24**, 743–751
4. Clabbers, M. T. B., Holmes, S., Muusse, T. W., Vajjhala, P. R., Thygesen, S. J., Malde, A. K., *et al.* (2021) MyD88 TIR domain higher-order assembly interactions revealed by microcrystal electron diffraction and serial femtosecond crystallography. *Nat. Commun.* **12**, 2578
5. Li, J., McQuade, T., Siemer, A. B., Napetschnig, J., Moriwaki, K., Hsiao, Y.-S., *et al.* (2012) The RIP1/RIP3 necrosome forms a functional amyloid signaling complex required for programmed necrosis. *Cell* **150**, 339–350
6. Mompeán, M., Li, W., Li, J., Laage, S., Siemer, A. B., Bozkurt, G., *et al.* (2018) The structure of the necrosome RIPK1-RIPK3 core, a human hetero-amyloid signaling complex. *Cell* **173**, 1244–1253
7. Wu, X., Ma, Y., Zhao, K., Zhang, J., Sun, Y., Li, Y., *et al.* (2021) The structure of a minimum amyloid fibril core formed by necroptosis-mediating RHIM of human RIPK3. *Proc. Natl. Acad. Sci. U. S. A.* **118**. e2022933118
8. Sun, X., Yin, J., Starovasnik, M. A., Fairbrother, W. J., and Dixit, V. M. (2002) Identification of a novel homotypic interaction motif required for the phosphorylation of receptor-interacting protein (RIP) by RIP3. *J. Biol. Chem.* **277**, 9505–9511
9. Mompeán, M., Chakrabartty, A., Buratti, E., and Laurents, D. V. (2016) Electrostatic repulsion governs TDP-43 C-terminal domain aggregation. *PLoS Biol.* **14**, e1002447
10. Tamiola, K., Acar, B., and Mulder, F. A. (2010) Sequence-specific random coil chemical shifts of intrinsically disordered proteins. *J. Am. Chem. Soc.* **132**, 18000–18003
11. Jumper, J., Evans, R., Pritzel, A., Green, T., Figurnov, M., Ronneberger, O., *et al.* (2021) Highly accurate protein structure prediction with AlphaFold. *Nature* **596**, 583–589
12. Pham, C. L., Shanmugam, N., Strange, M., O'Carroll, A., Brown, J. W., Sierecki, E., *et al.* (2019) Viral M45 and necroptosis-associated proteins form heteromeric amyloid assemblies. *EMBO Rep.* **20**, e46518
13. Vanden Berghe, T., Hassannia, B., and Vandenabeele, P. (2016) An outline of necrosome triggers. *Cell. Mol. Life Sci.* **73**, 2137–2152

14. Kaiser, W. J., and Offermann, M. K. (2005) Apoptosis induced by the toll-like receptor adaptor TRIF is dependent on its receptor interacting protein homotypic interaction motif. *J. Immunol.* **174**, 4942–4952
15. Steain, M., Baker, M. O. D. G., Pham, C. L. L., Shanmugam, N., Gambin, Y., Sierecki, E., *et al*. (2020) Varicella zoster virus encodes a viral decoy RHIM to inhibit cell death. *PLoS Pathog.* **16**, e1008473
16. Shanmugam, N., Baker, M. O. D. G., Sanz-Hernandez, M., Sierecki, E., Gambin, Y., Steain, M., *et al*. (2021) Herpes simplex virus encoded ICP6 protein forms functional amyloid assemblies with necroptosis-associated host proteins. *Biophys. Chem.* **269**, 106524
17. Duff, A. P., Wilde, K. L., Rekas, A., Lake, V., and Holden, P. J. (2015) Robust high-yield methodologies for (2)H and (2)H/(15)N/(13)C labeling of proteins for structural investigations using neutron scattering and NMR. *Methods Enzymol.* **565**, 3–25
18. Mészáros, B., Erdős, G., and Dosztányi, Z. (2018) IUPred2A: context-dependent prediction of protein disorder as a function of redox state and protein binding. *Nucleic Acids Res.* **46**, W329–W337
19. Erdős, G., and Dosztányi, Z. (2020) Analyzing Protein Disorder with IUPred2A. *Curr. Protoc. Bioinform.* **70**, e99
20. Ishida, T., and Kinoshita, K. (2007) PrDOS: prediction of disordered protein regions from amino acid sequence. *Nucleic Acids Res.* **35**, W460–W464
21. Jones, D. T., and Cozzetto, D. (2015) DISOPRED3: precise disordered region predictions with annotated protein-binding activity. *Bioinformatics* **31**, 857–863
22. Obradovic, Z., Peng, K., Vucetic, S., Radivojac, P., Brown, C. J., and Dunker, A. K. (2003) Predicting intrinsic disorder from amino acid sequence. *Prot. Struc. Funct. Gene.* **53**, 566–572
23. Hanson, J., Paliwal, K. K., Litfin, T., and Zhou, Y. (2019) SPOT-disorder2: Improved protein intrinsic disorder prediction by ensembled deep learning. *Gen. Proteomics Bioinform.* **17**, 645–656
24. Katuwawala, A., Ghadermarzi, S., Hu, G., Wu, Z., and Kurgan, L. (2021) QUARTERplus: Accurate disorder predictions integrated with interpretable residue-level quality assessment scores. *Comput. Struct. Biotechnol. J.* **19**, 2597–2606
25. Vuister, G. W., and Bax, A. (1993) Quantitative J correlation: a new approach for measuring homonuclear three-bond J(HNH.alpha.) coupling constants in 15N-enriched proteins. *J. Am. Chem. Soc.* **115**, 7772–7777
26. Shen, Y., Roche, J., Grishaev, A., and Bax, A. (2018) Prediction of nearest neighbor effects on backbone torsion angles and NMR scalar coupling constants in disordered proteins. *Protein Sci* **27**, 146–158
27. Shi, Z. S., Olson, C. A., Rose, G. D., Baldwin, R. L., and Kallenbach, N. R. (2002) Polyproline II structure in a sequence of seven alanine residues. *Proc. Natl. Acad. Sci. U. S. A.* **99**, 9190–9195
28. Roche, J., Maltsev, A. S., and Bax, A. (2013) Impact of hydrostatic pressure on an intrinsically disordered protein: a high-pressure NMR study of α-synuclein. *ChemBioChem* **14**, 1754–1761
29. Kjaergaard, M., Brander, S., and Poulsen, F. M. (2011) Random coil chemical shift for intrinsically disordered proteins: effects of temperature and pH. *J. Biomol. NMR* **49**, 139–149
30. Kjaergaard, M., and Poulsen, F. M. (2011) Sequence correction of random coil chemical shifts: correlation between neighbor correction factors and changes in the Ramachandran distribution. *J. Biomol. NMR* **50**, 157–165
31. Schwarzinger, S., Kroon, G. J., Foss, T. R., Chung, J., Wright, P. E., and Dyson, H. J. (2001) Sequence-dependent correction of random coil NMR chemical shifts. *J. Am. Chem. Soc.* **123**, 2970–2978
32. Lee, W., Tonelli, M., and Markley, J. L. (2015) NMRFAM-SPARKY: enhanced software for biomolecular NMR spectroscopy. *Bioinformatics* **31**, 1325–1327
33. Palmer, A. G., and Massi, F. (2006) Characterization of the dynamics of biomacromolecules using rotating-frame spin relaxation NMR spectroscopy. *Chem. Rev.* **106**, 1700–1719